ChemCatChem

Research Article
doi.org/10.1002/cctc.202402089

Chemistry Europe
European Chemical Societies Publishing

www.chemcatchem.org

Unlocking the Acidity-Reactivity Correlation of Metal(IV)-Doped Silica Nanotubes in the Conversion of Ethyl Levulinate

Martina Saitta,[a, b] Amélie Maertens,[a] Loraine Soumoy,[a] Anthony Morena,[a] Luca Fusaro,[a] Richa Tomer,[b] Marco Armandi,[c] Sonia Fiorilli,[c] Sophie Hermans,[b] and Carmela Aprile*[a]

Metal-doped hollow silica nanotubes (M-NT, where M = Ti, Zr, Hf) were successfully synthesized via a straightforward impregnation of pristine hollow silica nanotubes with M-acetylacetonate solutions. After their characterization, the materials were tested as heterogeneous catalysts for the conversion of ethyl levulinate (EL) into γ-valerolactone (GVL) revealing highly promising activity for the target reaction. Special emphasis was given on disclosing the influence of the nature of the acid sites (Lewis or Brønsted) and their strength on the catalytic performances. Ammonia temperature programmed desorption (NH_3-TPD), ^{31}P solid-state nuclear magnetic resonance (^{31}P-ssNMR) of trimethylphosphine and FT-IR of adsorbed ammonia, were the key techniques to evaluate the structure–activity correlation. The best solid exceeds the activity of other reference catalysts reported in the literature and tested under similar reaction conditions. The efficient recyclability of the best catalyst of the series was evaluated as well. The low E-factor obtained further confirmed the overall sustainability of the process.

1. Introduction

The valorization of low-cost lignocellulosic biomass constitutes a central research topic in the field of catalysis and sustainable chemistry.[1] Lignocellulose is composed of three main components, namely cellulose, hemicellulose (which makes up about 70% of the weight of dry lignocellulose biomass), and lignin.[2] From cellulose, through a series of catalyzed reactions, it is possible to obtain high-value platform molecules such as γ-valerolactone (GVL).[3] This compound can be classified as "green solvent" (i.e., liquid compound with low toxicity, high stability, biodegradability, and enhanced solubilizing power).[4] Moreover, GVL can be employed as precursor for the production of fuel additives (e.g., valeric esters) and polymers (e.g., α-methylene-γ-valerolactone).[5]

Within the overall catalytic process, γ-valerolactone can be obtained by reduction of levulinic acid or its esters (derived directly from cellulose),[6] like ethyl levulinate (EL), using molecular H_2 in the presence of a noble metal-based catalyst (e.g., Ru, Pd, Ir)[7] or via the in situ hydrogenation using Pd-based catalysts.[8] These approaches allow reaching high yields in GVL, but they present different drawbacks mainly related to the high cost of noble metals and the harsh reaction conditions applied. While the first drawback can be overcome employing catalysts embedding non-noble metals (e.g., Ni, Cu, Mg, Al),[9] the second one could be faced carrying out an alternative and more environmentally friendly route, such as the catalytic transfer hydrogenation (CTH) process,[10] also known as Meerwein–Pondorf–Verley reduction. In this process, an alcohol is used as H-donor to reduce the levulinic ester, under milder conditions by comparison with the H_2 pathway. CTH is usually carried out in the presence of homogeneous or heterogeneous Lewis acid catalysts. A combination of Brønsted (B) and Lewis (L) acidity was also reported to be beneficial for the target reaction.[11] In general, the easy recyclability of heterogeneous catalysts makes them better candidates from a sustainability point of view, since they can be easily separated from the reaction mixture by filtration or centrifugation and readily used over multiple cycles.

The most representative catalysts, previously reported in the literature for the conversion of EL to GVL through a catalytic transfer hydrogenation process, are ZrO_2,[12] ZrO_2 supported on different solids (e.g., ZrO_2/zeolites,[13] ZrO_2/SBA-15,[14] ZrO_2/graphene oxide[15]) and Zr-MOFs.[16] Hierarchical zeolites, hence displaying also mesoporosity, doped with different metals recently showed promising results as well.[17] Among the broad class of mesoporous materials, it was recently shown by our group that hollow silica nanotubes (NT), synthesized via a sol–gel approach[18] and then impregnated with Zr(IV) species, are promising catalysts for the aforementioned reaction.[18] The high activity of the Zr-NT, displaying a Si/Zr ratio of 74, was attributed

[a] M. Saitta, A. Maertens, L. Soumoy, A. Morena, L. Fusaro, C. Aprile
Laboratory of Applied Materials Chemistry, UCNANO, Department of Chemistry, Namur Institute of Structured Matter (NISM), University of Namur, Namur 5000, Belgium
E-mail: carmela.aprile@unamur.be

[b] M. Saitta, R. Tomer, S. Hermans
Institute of Condensed Matter and Nanosciences (IMCN), Université catholique de Louvain (UCLouvain), Place Louis Pasteur, 1, Louvain-la-Neuve 1348, Belgium

[c] M. Armandi, S. Fiorilli
Department of Applied Science and Technology, Politecnico di Torino, Torino 10129, Italy

Martina Saitta, Amélie Maertens, and Loraine Soumoy contributed equally to this work.

Supporting information for this article is available on the WWW under https://doi.org/10.1002/cctc.202402089

to a favorable combination of structural and acidity features (open structure and optimal L/B acid balance). However, other key parameters such as the Si/M ratio or the nature of the metal cation (M) were not considered.

In the context of zeolite-based solids, it is known that the nature of the doping element can impact the acidic properties and therefore significantly influence the activity of the catalyst.[19] Among the different tetravalent elements already encountered in the context of silica based heterogeneous acid catalysts, Hafnium has shown highly promising results. Its beneficial role for the conversion of ethyl levulinate to γ-valerolactone was reported by Wu et al. with acid-base bi-functional solid catalysts. The Brønsted acid sites introduced by the presence of Hf favors the adsorption of the substrate on the surface of the catalyst and thus enhances the catalytic activity.[20] Titanosilicates also displayed promising catalytic results for various catalytic processes. Their performances were generally ascribed to their high Lewis acidity. For example, Ti-containing heterogeneous materials presenting highly dispersed Ti(IV) species on the SiO_2 surface are catalysts of choice for the industrial production of propylene oxide by Shell company.[21] Significative improvements were later made on this process with the development of titanium silicalite-1 (TS-1), a Ti-containing zeolite.[22] The use of Ti-based silica materials for the valorization of EL to GVL was less explored, and, when considered in a catalytic screening, titanosilicates were less active than other metal active centers for the overmentioned reaction.[11] However, when combined with zirconium in mixed oxide solids (e.g., in the proportion Ti:Zr 2:8), full conversion is reached within 6 h while only 86% and 16% were obtained with pure mesospheric zirconium and titanium oxide respectively.[23] Enhanced catalytic performances were also observed with Zr species supported on TiO_2 nanoparticles.[24] A systematic study of the activity of Ti-, Zr-, and Hf-zeolites towards the conversion of methyl levulinate to GVL was performed by Luo et al.[17b] The work consisted of a catalytic screening employing zeolites possessing M^{4+} centers incorporated into the framework. The authors found out that Hf-based zeolites were the best of the series in terms of reaction rates, but they did not correlate this catalytic behavior with the acidity of the catalysts. However, to the best of our knowledge a systematic study on mesoporous metallosilicates was not performed yet.

Tubular nanomaterials have been largely employed in biomass valorization because of their unique features,[25] such as high specific surface area, good accessibility to the active sites and the possibility of functionalizing their surface to tune their chemical properties.[26] Halloysite clay nanotubes were also efficiently employed as catalysts in the valorization of biomass.[27] In this work, we propose hollow silica nanotubes post-impregnated with Ti, Zr, and Hf oxides as efficient catalysts for the conversion of EL into GVL. The three aforementioned metals are part of the earth abundant metal (EAM) highlighted in a recent review by Bullock et al.[28] A preliminary screening on the Si/M ratio (37, 74, and 110) was performed with Zr-NT. The optimal Si/Zr ratio was selected for in-depth investigation and its activity compared with Ti-NT and Hf-NT displaying the same Si/M ratio. All the solids were extensively characterized by N_2 physisorption, transmission electron microscopy, and X-ray photoelectron spectroscopy. The characterization of the acidity of the solids was carried out using complementary techniques, namely temperature programmed desorption (TPD) of ammonia, Fourier-transform infrared spectroscopy (FT-IR) of ammonia, and ^{31}P solid state nuclear magnetic resonance (^{31}P ss-NMR) of trimethylphosphine (TMP), employed as probe molecule. These characterizations revealed that the total amount of acid sites as well as the Lewis/Brønsted (L/B) ratio were the crucial parameters to explain the structure–activity correlation for this series of solids. In addition, a clear dependence of catalytic activity on the strength of the acid site was observed hence adding a key milestone to the overall understanding of the process.

2. Materials and Methods

2.1. Materials

Tetraethoxysilane (TEOS, 97%) and decane (analytical grade) were purchased from TCI. Solutions of ammonia 30%, HCl 2 M, HCl 37%, HNO_3 69%, HF 48% and 2-propanol were purchased from Carl Roth. Zirconium acetylacetonate ($Zr(acac)_4$, 97%) was purchased from Alfa Aesar. Absolute ethanol came from Fisher Scientific (analytical grade). Ethyl levulinate and Pluronic F127 were purchased from Sigma Aldrich. Titanium diisopropocide bis(acetylacetonate) ($Ti(acac)_2(OiPr)_2$, 75% in isopropanol) and hafnium acetylacetonate ($Hf(acac)_4$, 97%) came from Thermo Scientific.

2.2. Synthesis of NT

The synthesis of hollow silica nanotubes (NT) was carried out following a procedure previously reported in the literature by Soumoy et al.[29] The synthesis was performed in a fridge (Aqualytic TC 140 G Model) at 12 °C, inside a 250 mL covered glass vessel (70 mm in diameter and 133 mm in height). 60.0 mL of HCl 2 M were added to 1.0 g (0.160 mmol) of Pluronic F127. The mixture was magnetically stirred at 250 rpm (stirring bar: 6 mm in diameter and 30 mm in length) for 1 h to solubilize the templating agent. Then, 3 mL of toluene and 2.8 g (13 mmol) of tetraethyl orthosilicate were added dropwise to the templating agent solution. After 24 h, 10.5 mL of an ammonia solution (30 wt.%) were added to the mixture to reach a pH of 9. The reaction mixture was then stirred for another 24 h at 12 °C. After filtration and washing with distilled water (500 mL), the resulting gel was dried at 65 °C. The collected powder was finally calcined in air at 550 °C for 5 h with a heating rate of 2 °C/min.

2.3. Post-Synthesis Doping to Obtain M-NT Materials

Hollow silica nanotubes were synthesized following the procedure described above. After the calcination treatment, the NTs were impregnated with a solution of metal precursor, as described below.

Zr-NT: Three materials were synthesized, targeting a Si/Zr ratio of 37, 74, 110. To do so, 110 mg (0.225 mmol), 55 mg

(0.113 mmol) or 37 mg (0.076 mmol) of $Zr(acac)_4$ were solubilized respectively in 4, 2, or 1.3 mL of absolute ethanol and 800, 400 or 270 µL of distilled water. The so-formed solution was then added dropwise to 500 mg of NTs (8.32 mmol). The slurry was manually stirred (ca. 5 min) and then dried at 65 °C. The solid was subsequently calcined at 550 °C for 5 h (heating rate: 2 °C/min). The samples were labeled Zr-NT-x, where "x" is the Si/Zr ratio.

Ti-NT: 37 µL (0.076 mmol) of $Ti(acac)_2(O^iPr)_2$ were diluted in 2.5 mL of absolute ethanol. This solution was added dropwise to 500 mg of NTs (8.32 mmol). The same procedure as for the preparation of Zr-NT was carried out for the next steps.

Hf-NT: 44 mg (0.076 mmol) of $Hf(acac)_4$ were solubilized in 1.6 mL of absolute ethanol and 320 µL of distilled water. The solution was added dropwise to 500 mg of NTs (8.32 mmol). The same procedure as for the preparation of Zr-NT was carried out for the next steps.

2.4. Characterization Techniques

Transmission electron microscopy (TEM) was performed with a Philips Tecnai 10 device operating at 80 kV. The solids were dispersed in absolute ethanol and deposited on a Formvar–Copper grid.

The total amount of metals in the samples was determined via Inductively coupled plasma optical emission spectroscopy (ICP-OES) on an Optima 8000 Spectrometer after dissolution of 10 mg of the solid by an aqueous solution of HCl 37%, HNO_3 69%, and HF 48%. The errors associated to the measurements were less than the 2% of the given values.

N_2 adsorption–desorption analyses were performed at 77 K with a Micromeritics ASAP 2420 volumetric adsorption analyzer. Before starting the analysis, degassing of the samples (8 h, 150 °C) under reduced pressure (0.1 mbar) was carried out. To evaluate the specific surface area, the Brunauer–Emmet–Teller (BET) method was applied in the 0.05–0.30 P/P_0 range. Pore size distributions (PSD) were assessed from the adsorption branch of the isotherm, applying the Barrett–Joyner–Halenda (BJH) method with the Kruk–Jaroniec–Sayari (KJS) correction. To better determine the internal porosity, HR-TEM measurement were performed as well. The maximum expected percent uncertainty in specific surface area values is 10%.

X-ray photoelectron spectroscopy (XPS) measurements were carried out on a Thermo Fisher ESCALAB 250Xi spectrometer, with a hemispherical deflector analyzer working at fixed pass energy (150 eV for survey spectra and 20 eV for high-resolution spectra) and a monochromatic Al Kα X-ray source (1486.6 eV). The X-ray spot diameter was set at 300 µm. To compensate the charges induced by the emission of photoelectrons, a flood gun, using electrons and Ar ions, was used. High resolution photoemission spectra of every species present in the materials were fitted with Gaussian-Lorentzian lineshape. Binding energies were referenced to the C—C feature of the C1s line at 284.8 eV. The error associated to the binding energies values was 0.1 eV.

Temperature-programmed desorption of ammonia (NH_3-TPD) analysis started by introducing the samples in a quartz reactor on a Hiden Analytical Catlab gas analyzer coupled with QGA Hiden Analytical quadrupole mass spectrometer. Prior to the analysis, the sample (20–30 mg) was dried under air flow (30 mL min^{-1}) at 550 °C for 2 h. Then it was cooled down to 60 °C and exposed to a gas mixture of 5% NH_3 in He (15 mL min^{-1}) and Ar (15 mL min^{-1}) for 60 min. A purge with Ar (30 mL min^{-1}, 90 min, 60 °C) was carried out to evacuate the physisorbed NH_3. The TPD analysis was performed by heating the sample from 60 to 550 °C with a heating rate of 10 °C min^{-1}. Desorbed NH_3 was detected via mass spectrometry (QGA model). The total acidity was calculated on the basis of integral area of the respected peaks obtained from molecules desorbed per sec versus desorption temperature curve.

FT-IR measurements were conducted in transmission mode by using a Bruker Tensor 27 spectrometer. The liquid nitrogen-cooled mercury–cadmium–telluride (MCT) detector was operating at a 2 cm^{-1} resolution. Analyses and pre-treatment (outgassing under high vacuum for 1 h at 673 K) were carried out in an IR cell equipped with KBr windows. Samples were pressed in a self-standing wafer which displayed similar optical density for all samples (ca. 5 mg cm^{-2}). FT-IR spectra were recorded after dosing ammonia on the pre-treated samples, at the maximum equilibrium pressure of 2000 Pa. The equilibrium pressure was then progressively decreased, and spectra were recorded sequentially. Finally, samples were outgassed for ca. 30 min. The registered spectra were normalized to the integrated absorption of the silica framework overtone bands and the reported difference spectra were obtained after subtraction of the IR spectrum of the bare sample, before ammonia adsorption.

Solid-state ^{31}P MAS NMR spectra were obtained at ambient temperature using a 400 MHz Varian VNMRS spectrometer operating at 9.4 T (161.9 MHz for ^{31}P), equipped with a 4 mm Varian/Chemagnetics T3 probe. The samples were packed into a 4 mm bio solids cavern rotor fitted with a nonvented top cap made of PCTFE and equipped with two o-rings. MAS spectra were recorded at a spinning frequency of 8 kHz. A $\pi/2$ flip-angle of 3.4 µs, a relaxation delay of 6 s, an acquisition duration of 20 ms, and a total of 1280 scans were employed to gather the single-pulse ^{31}P MAS NMR spectra. Decoupling on the ^1H channel (TPPM) was performed with B_1 set to 27.7 kHz. Chemical shifts were referenced externally to ammonium dihydrogen phosphate ($(NH_4)H_2PO_4$) (^{31}P: 0.81 ppm).[18] A portion of the sample was dehydrated in two stages. Initially, it was calcined at 550 °C for 8 h, followed by placing the sample under vacuum (10^{-3} mbar) in a Schlenk line system for 1 h. The 4 mm rotor was filled with the solid in an inert atmosphere (Ar) within a glovebox, and 2 or 2,5 µL of trimethylphosphine (TMP) in liquid form was introduced into the rotor. The removal of excess TMP was executed using a homemade setup similar to one documented in the literature.[18] The rotor was secured in a holder connected to a vacuum line and an oven, subjected to a vacuum of 10^{-6} mbar for 45 min or1 h at 100 °C. All the spectra were processed using *MestreNova (V6.0.2)* software applying phase and baseline corrections, and an exponential apodization of 100 Hz.

The obtained spectrum of the solid Hf-NT-110 using the previous reported condition, was processed 10 times using two different softwares: MestreNova (V6.0.2) and VNMRJ (V3.1). Each time a slight variation on phase parameters and on the baseline

correction was applied. After the processing step, all the spectra were plotted in Origin (V2017). The software was used to deconvolute the spectra and estimate the areas of the peaks. Gaussian fitting was applied in each case, using three reference peak centers: (i) a peak at −4.6 ppm, (ii) a peak at −35.5 ppm, and (iii) a variable contribution within the range of −10 to −20 ppm, depending on the spectrum. The resulting values were used to calculate the final Lewis-Brønsted ratio of the solid.

2.5. Conversion of Ethyl Levulinate to γ-Valerolactone

The catalytic tests were performed in a 10 mL Schlenk flask at atmospheric pressure (as initial pressure). 142 µL of ethyl levulinate (1 mmol), 25 µL of decane (GC internal standard), 100 mg of freshly calcined catalyst and 5 mL of 2-propanol were introduced in the Schlenk flask. The flask, after sealing, was immersed in an oil bath, previously heated at 150 °C (time "0"). The mixture was left under magnetic stirring at 800 rpm for the selected time. After cooling, 500 µL of the reaction mixture were withdrawn and centrifuged (4500 rpm, 5 min). The supernatant was collected, diluted 1:1 in absolute EtOH and analyzed via GC-FID equipped with a Stabliwax Restek GC column. The GC analysis was performed following a temperature program of 1 min at 50 °C, 10 min with a ramp of 20 °C/min until 250 °C, 3 min at 250 °C. To calculate the yield and the conversion, the amount of GVL and ethyl levulinate in the mixture were determined from calibration lines (R^2_{GVL} 0.9985, R^2_{EL} 0.9981). Selectivity was obtained from conversion and yield.

2.6. Recycling of Catalyst

The recycling experiments were carried out following the same procedure as a regular test (see Section 2.5). The reaction mixture was filtered after 3 h. The liquid part was analyzed via GC-FID, while the collected solid was dried at 65 °C and then calcined at 550 °C for 5 h (heating rate: 2 °C/min). The procedure was repeated for the following cycles, scaling down the amounts of reactants used on the basis of the quantity of catalyst recovered.

2.7. E-Factor

To evaluate the E-factor, a regular catalytic test was performed (see Section 2.5). The reaction was stopped after 24 h and the reaction mixture was transferred into a round-bottom flask, connected to a micro-distillation apparatus to recover the solvent.

3. Results and Discussion

3.1. Zirconium(IV)-Doped Silica Nanotubes: Synthesis, Characterization, and Catalytic Results

The synthesis of silica nanotubes (NT) was performed by optimizing a procedure recently reported in the literature.[29,30] A post-synthesis approach was employed to obtain finely dispersed EAM oxides at the surface of silica nanotubes. The final materials were denoted as M-NT (M = Ti^{4+}, Zr^{4+}, Hf^{4+}). A preliminary screening was performed to evaluate the impact of the Si/M ratio. To this purpose, a series of Zr-NTs displaying an increasing quantity of surface zirconium species was synthesized. The samples are denoted Zr-NT-*x*, where x is the theoretical Si/Zr ratio. The total amount of zirconium, assessed via Inductively coupled plasma-optical emission spectroscopy (ICP-OES), after solubilization of the samples, revealed an excellent agreement with the nominal composition of the different solids (see Table 1). The morphology and the textural features of the materials were probed via transmission electron microscopy (TEM) and N_2 physisorption. Due to the very similar features, only the results relative to Zr-NT-110 are presented herein. Zr-NT-74,[18] was added for comparison. The characterization of the other solid of the series is available in the Supporting Information (S1–S3). All the materials displayed a tubular structure randomly organized (Figure 1a,b). Their internal diameter and walls thickness were respectively of about 14 nm and 4 nm, in accordance with previous research carried out in the group.[29,31] The steep N_2 uptake in the adsorption isotherms (see Figure 1c) at low relative pressure (ca. $p/p° = 0.02$) indicated the presence of micropores in the walls, while the pore condensation which takes place at higher relative pressure (ca. $p/p° = 0.8$) was ascribed to the presence of wide mesopores, i.e., the internal void of the tubes. While the morphology of the tubes, as visualized by TEM, did not change when varying the amount of metal oxide in the materials, the Brunauer–Emmett–Teller (BET) specific surface area and the pore volume of the nanostructures slightly decreased when increasing the Zr content (see Table 1). This phenomenon could be due to the presence of a larger amount of ZrO_2 species at the outer surface of the tubes partially clogging the micropores or the small mesopores present within the walls. Indeed, the pore diameters were assessed by the BJH (Barrett–Joyner–Halenda)-KJS (Kruk–Jaroniec–Sayari) method. The broad distribution obtained via BJH can be considered as the result of different contributions coming from the mesopores present in the silica walls, the internal nanotube diameter and the interparticle porosity generated by the entangled nature of the tubular aggregates. Hence, a precise value of the internal pore diameter for each sample of NTs cannot be directly estimated from this plot. A more correct evaluation of the internal diameter (reported in Table 1) can be obtained from HR-TEM analysis. The average value of the distribution derived from TEM investigation is also reported in Figure S4. The internal pore diameter, assessed by TEM did not suffer from any relevant decrease, remaining constant throughout the series (ca. 14 nm).

To understand how the metal cations interacted with the pre-existing silica nanostructure, X-ray photoelectron spectroscopy (XPS) analyses were performed. The XPS spectra of the samples (Figure S3) were compared with the ones of pure ZrO_2, which presents the Zr $3d_{5/2}$ band at 182.0 eV, in accordance with what is reported in literature.[32] As presented in Table 1, the Zr binding energies (BE) observed for this first series of samples were all shifted towards higher values compared to commercially available ZrO_2, indicating that the Zr species were experiencing a

Table 1. Characterization data of Zr-NT-x (x = 37, 74, 110) samples.

Entry	Sample	S_{BET} (m^2/g)	Pore Volume (cm^3/g)	Internal Diameter[a)] (nm)	Si/Zr (via ICP-OES)	Binding Energy Zr 3d $_{5/2}$ (eV)
1	**NT**	575	2.1	14	–	–
2	**Zr-NT-37**	478	1.7	14	39	182.9
3	**Zr-NT-74**	489	1.9	14	73	183.2
4	**Zr-NT-110**	498	1.9	13	108	183.0

[a)] The reported values were determined via TEM distribution.

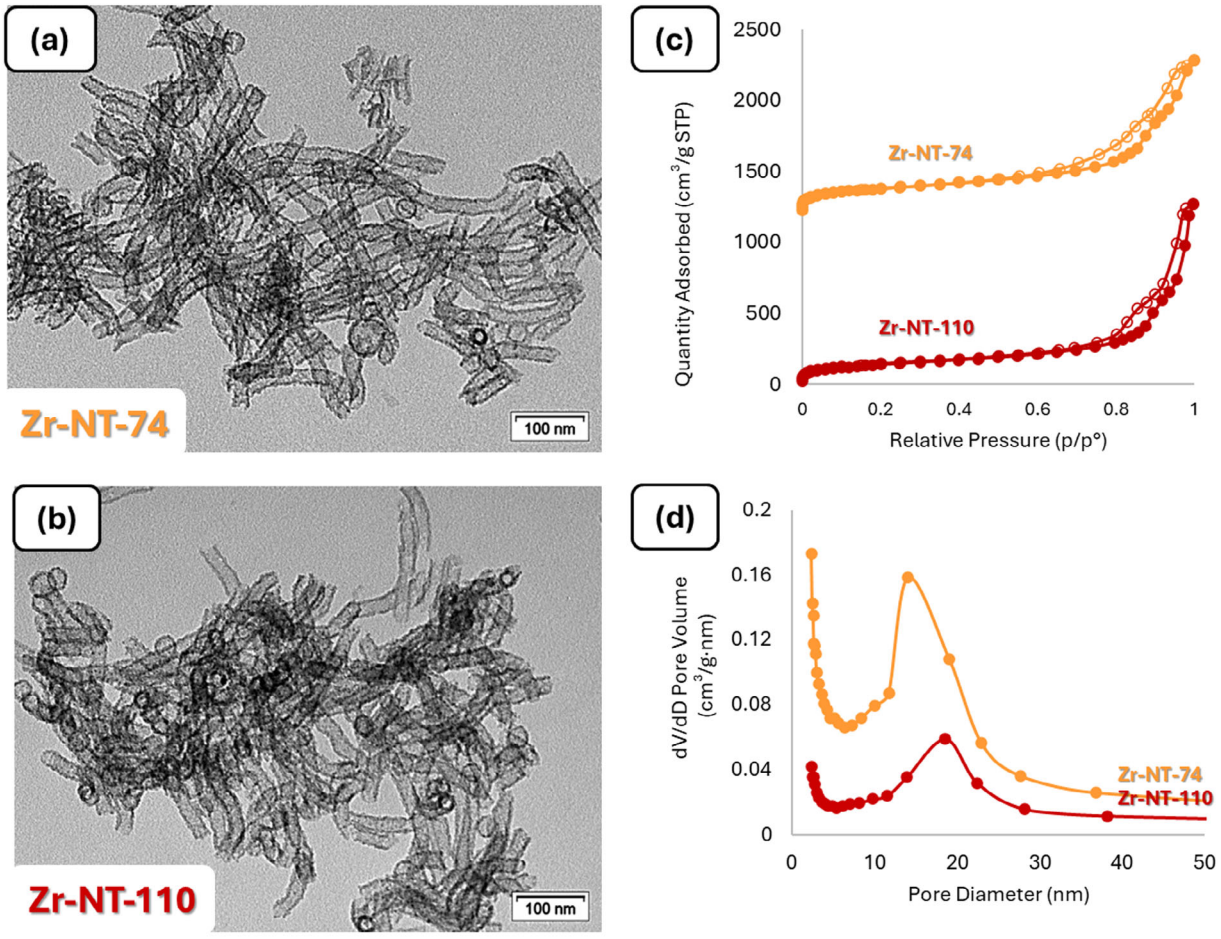

Figure 1. TEM images of (a) Zr-NT-74 and (b) Zr-NT-110. (c) Nitrogen physisorption isotherms of Zr-NT-74 (for clarity, the second isotherm was shifted of 1200 cm^3/g) and Zr-NT-110. (d) BJH-KJS pore size distribution of Zr-NT-74 and Zr-NT-110 samples.

different chemical environment once dispersed at the surface of silica nanotubes. The shift towards higher binding energy could be ascribed to the higher electronegativity of silicon compared to zirconium, resulting in a lower electronic density on the Zr metal centers. This suggested that the Zr centers present at the surface of the clusters were strongly interacting with silica.

The synthesized solids displayed textural and chemical properties that made them suitable candidates for heterogeneous catalysis. The catalytic performances of the solids of the Zr-NT-*x* series were tested selecting the conversion of ethyl levulinate to γ-valerolactone as target reaction. The catalytic process was performed using 2-propanol both as H-donor and solvent. In Table 2, the catalytic results obtained with the three Zr-NT solids are reported, as well as two additional blank tests carried out using pristine silica nanotubes (Entry 1) and commercially available zirconia (Entry 2). The yield of both blank tests was inferior to 2%, proving that zirconium sites are essential to confer catalytic activity to silica nanotubes and that the fine dispersion of metal oxide at the surface of the NT leverages the catalytic activity. All the samples of the Zr-NT series displayed relevant catalytic performances in the selected reaction. It is important to note that under these conditions, the transesterification side-reaction leading to the production of iso-propyl levulinate occurred as well, explaining the moderately low values of the selectivity observed in particular for Zr-NT-37. Due to the different Zr loading, a suitable comparison could only be made considering the Turnover

Table 2. Catalytic activity of Zr(IV)-doped silica nanotubes in the conversion of ethyl levulinate to GVL.

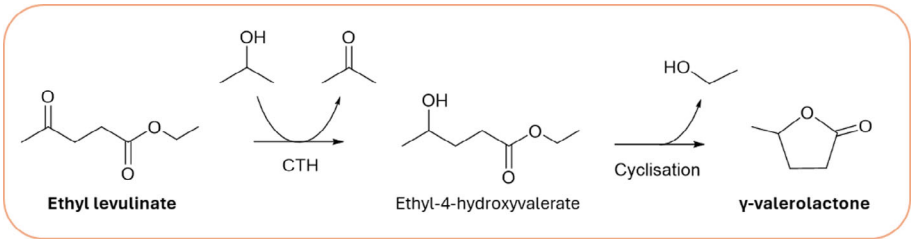

Entry	Catalyst	Conversion (%)	Yield (%)	Sel. (%)	TON
1	NT	<2	<2	n.a.	n.a.
2	ZrO_2	<2	<2	n.a.	n.a.
3	Zr-NT-37	40	20	49	5
4	Zr-NT-74	29	19	66	9
5	Zr-NT-110	26	21	83	14

Conditions of the catalytic tests: 100 mg of catalyst, 150 °C, 3 h, 1 mmol of EL and 5 mL of ^{i}PrOH. Entry 2: 5.3 mg (4.3×10^{-5} mol) of commercial ZrO_2, 150 °C, 3 h, 1 mmol of EL and 5 mL of ^{i}PrOH. The error on the yield does not exceed 2% in absolute value. Sel. = Selectivity. TON = n_{GVL}/n_{Zr}; the amount of Zr within the Zr-doped samples was determined via ICP-OES analyses (Zr-NT-37: 4.1×10^{-4} mol/g, Zr-NT-74: 2.2×10^{-4} mol/g, Zr-NT-110: 1.5×10^{-4} mol/g). n.a.: not applicable.

Number (TON, defined as moles of GVL/moles of Zr determined via ICP-OES) values reported in Table 2. The results showed that increasing the quantity of Zr in the samples did not result in an enhancement of the catalytic activity as the lowest TON value was obtained employing the Zr-NT-37 catalyst. This result could be tentatively ascribed to the presence of larger ZrO_x clusters resulting from the higher quantity of zirconium immobilized on silica NTs. Even though no crystalline species were visible via XRD (see Figure S5) and no significant difference in terms of chemical environment was identified by XPS (see Table 1), it cannot be excluded that in Zr-NT-37 part of the zirconium was confined at the core of larger Zr—O—Zr clusters and therefore not accessible to reagents. Zr-NT-110 was the best performing catalyst with the highest TON of the series. This solid displayed a very similar conversion than Zr-NT-74 and a higher selectivity despite the lower amount of Zr. To better understand the reason for the different catalytic behavior of these two solids, acidity measurements were performed as well. The acidity of both Zr-NT-74 and -110 was determined by recording ^{31}P Direct Excitation ssNMR (DE-ssNMR) spectra of adsorbed trimethylphosphine (TMP). Through this technique it was possible to evaluate the presence of Lewis and Brønsted sites within the solids and to determine the L/B ratio by integration of the different contributions. Brønsted sites were most probably generated from the interaction between the Zr species and the silica via bridged silanol groups present at the surface of NTs.[18] Lewis acidity could be ascribed to the presence of unsaturated Zr cationic species at the surface of the ZrO_x clusters. The spectra of the TMP adsorbed on the two materials (see Figure 2) present a peak centered at c.a. −5 ppm which could be assigned to Brønsted sites.[33] The contribution related to Lewis acid sites could be observed in the region comprised between −30 and −60 ppm.[34] For Zr-NT-74, a single contribution centered at −43.8 ppm was observed. In contrast, Zr-NT-110 exhibited two distinct signals, one at −44.5 ppm and

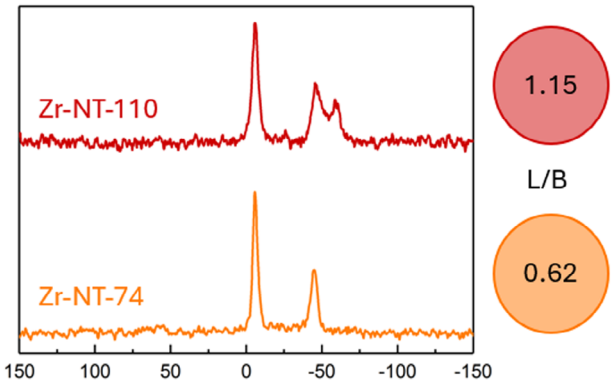

Figure 2. ^{31}P-ssNMR spectra of trimethylphosphine adsorbed on Zr-NT-74 and Zr-NT-110.

the other centered at −57.5 ppm, corresponding respectively to medium-strength and low-strength Lewis acid sites. The difference between the two spectra could be attributed to the higher heterogeneity of the active sites in Zr-NT-110 than in Zr-NT-74. Moreover, integrating the signals related to the two types of acidities, it was possible to calculate the L/B ratio for Zr-NT-110 and for Zr-NT-74, that were respectively 1.15 and 0.62. The higher L/B ratio of Zr-NT-110 could be related to the smaller size of the clusters (hence to higher quantity of coordinatively unsaturated Zr sites) and explains its better catalytic activity in comparison with Zr-NT-74 which most probably displays larger cluster (lower coordinatively unsaturated sites hence decreased L/B ratio). It is known that the formation of the desired product should be favored by high L/B.[17a,35] Moreover, this evidence allowed assessing that a Si/Zr ratio of 110 was the best compromise between a fine dispersion of the active sites and the necessary amount of metal oxide to catalyze the conversion of ethyl levulinate to γ-valerolactone.

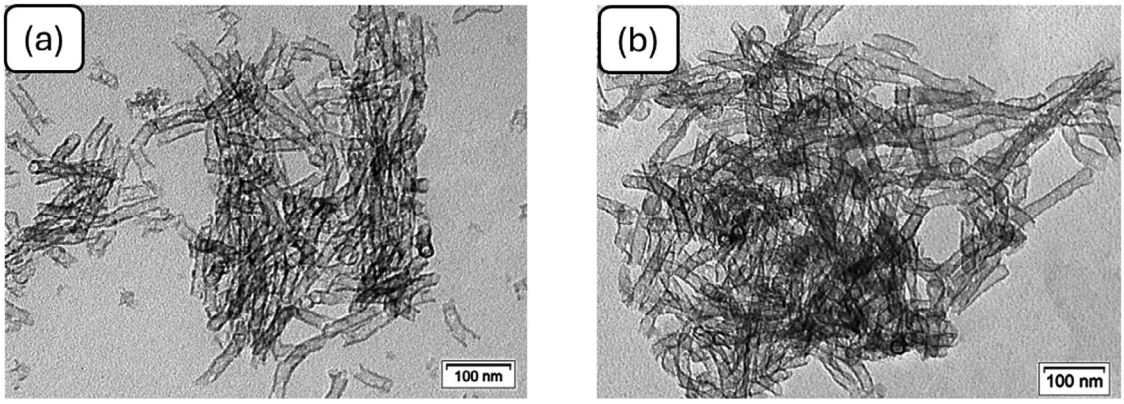

Figure 3. TEM images of (a) Hf—NT-110 and (b) Ti—NT-110.

Table 3. Characterization data of Ti-NT-110, Zr-NT-110, and Hf-NT-110.

Entry	Sample	S_{BET} (m^2/g)	Pore Volume (cm^3/g)	Internal Diameter[a] (nm)	Si/M (via ICP-OES)	Acid Sites TPD (μmol/g)	T_{max} TPD (°C)	L/B (via ^{31}P-ssNMR)
1	**NT**	575	2.1	14	–	–	–	–
2	**Ti-NT-110**	572	2.0	14	100	44	150	1.63
3	**Zr-NT-110**	498	1.9	13	108	37	210	1.15
4	**Hf-NT-110**	469	1.7	12	106	47	210	1,54 ± 0,17[b]

[a] The reported values were determined via TEM distribution (see Figure S6).
[b] See experimental part.

3.2. M(IV)-Doped Silica Nanotubes: Synthesis, Characterization, and Acidity Assessment

As mentioned above, the nature of the M^{4+} elements selected to impregnate the surface of silica nanotubes could strongly influence the catalytic activity by modifying the acidity of the surface. To investigate this correlation and to enhance the understanding of the key parameters governing the conversion of ethyl levulinate into GVL, two additional materials bearing titanium and hafnium were synthesized via a similar impregnation procedure as the one employed for Zr-NT-x. In agreement with the outcome of the optimization of the Si/Zr ratio, a Si/M ratio of 110 was targeted. The newly obtained solids were characterized through similar techniques as described above. The morphology of the nanotubes was not impacted by the presence of different metal cations. The tubes maintained their open structure and entangled organization as highlighted in Figure 3. As expected, the BET specific surface area (S_{BET}) of the NTs slightly decreased in comparison with the one of the pristine silica nanotubes (compare Entry 1 with Entries 2 and 3 of Table 3, Figure S7).

The ICP-OES results of the newly synthesized solids were in agreement with the theoretical value of Si/M = 110 (see Table 3). Finally, the XPS measurements indicated that both Ti^{4+} and Hf^{4+} species were interacting with the silica structure in the materials, since the spectra of Ti—NT-110 and Hf-NT-110 evidenced a significant shift of both the BE of the Ti $2p_{3/2}$ peak (459.7 eV) and the Hf $4f_{5/2}$ peak (19.3 eV) if compared to the ones of the corresponding pure oxides (TiO_2 Ti $2p_{3/2}$ = 458.3, HfO_2 Hf $4f_{5/2}$ = 18.4) (see Figure S8 for more details).

To unveil the correlation between the nature of the metal oxide and their activity, acidity measurements were carried out on the materials of the M—NT-110 series. Temperature programmed desorption (TPD) of ammonia was performed to evaluate how the nature of the metal (M) influenced the acidity of the material, both in terms of overall amount and strength. It emerged from TPD analyses (Table 3) that Ti—NT-110 presented active sites characterized by weak acidity, as evidenced from the temperature value where the maximum of the band lays (see Figure S9). Zr-NT-110 and Hf—NT-110 displayed similar medium-strength acid sites with the latter exhibiting slightly higher overall acidity if compared to Zr-NT-110 (Table 3). The higher population of acid sites could be tentatively ascribed to a better dispersion at the surface with the consequent formation of smaller metal oxide clusters which in turn could display a higher quantity of unsaturated M^{4+} species (responsible for higher Lewis acidity).

To prove this hypothesis and evaluate the Lewis over Brønsted ratio of the acid sites, TMP assisted ^{31}P DE-ssNMR was employed. The spectra reported in Figure 4 were recorded after careful evacuation of the excess of TMP. All the solids presented a peak centered at c.a. −5 ppm, ascribed to the Brønsted acid sites.[33] A clear difference was evident in the range of signals related to Lewis acidity, between −20 and −60 ppm.[34] The more evident difference is presented by the Ti-NT-110 sample. Indeed, despite the careful control of the condition to avoid

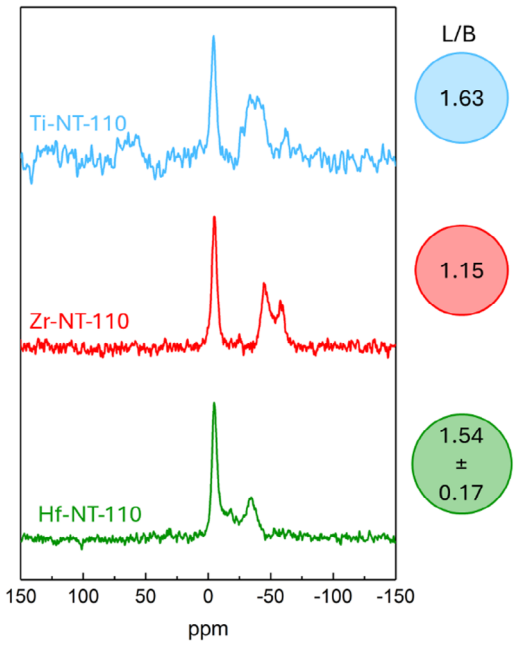

Figure 4. ^{31}P-ssNMR spectra of trimethylphosphine adsorbed on Ti—NT-110, Zr-NT-110, and Hf—NT-110.

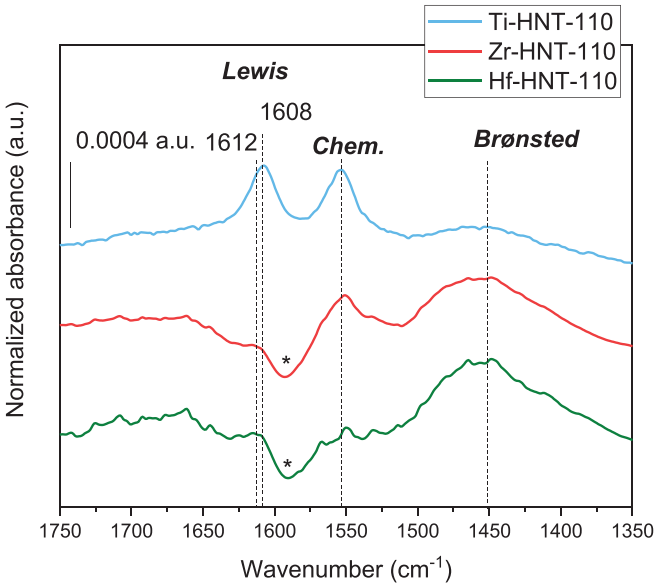

Figure 5. FT-IR difference normalized spectra of Ti—HNT-110, Zr—HNT-110, Hf—-NT-110 after ammonia adsorption and prolonged outgassing.

oxidation, Ti-NT-110 was the only sample displaying a small contribution at 57 ppm arising from the partial oxidation of TMP bonded to weak Lewis sites to form the corresponding trimethylphosphine oxide (TMPO).[36] Under the optimized protocol employed to adsorb TMP on the solids (see Experimental Section), unwanted oxidation can be ascribed to the weaker nature of the acid sites. This result was in agreement with the weak nature of the acid sites evidenced via TPD analysis. As expected, Zr-NT-110 and HfNT-110 possessed more similar acidic strength and no oxidation to TMPO was detected (Figure 4). Interestingly, Hf-NT-110 displayed stronger Lewis sites (laying from −17 to −35 ppm) than Zr-NT-110 (−50 and −60 ppm). The L/B ratio evaluated for the M—NT-110 series is indicated in Figure 4. Ti-NT-110 was the sample presenting the weakest acid strength, according to NH_3 TPD measurements, and the higher L/B ratio (1.63), assessed via ss-NMR. The L/B ratios evaluated for Zr-NT-110 and Hf-NT-110 were 1.15 and 1.54 ± 0.17, respectively. The strong nature of the Lewis sites observed for Hf-NT-110 made the correct quantification of the Lewis over Brønsted acidity particularly delicate. As can be seen in Figure 4, the L contributions overlapped with those related to B acid centers, necessitating a preliminary deconvolution step. To this purpose, it is important to consider that many parameters as baseline correction and phase adjustment procedures can significantly impact the estimation of the area of these large signals. To reduce the possible errors and to give a more precise quantification of the L/B ratio, the integrated areas of interest were estimated after a series of ten different processing and plotting steps (see Experimental Section). This procedure allowed estimating the error in processing and evaluating correctly the L/B ratio.

The conclusion that could be drawn after these analyses was that the solids displaying a higher quantity of acid sites (from TPD-NH_3 analysis) also presented a higher proportion of Lewis acidity (evaluated via ssNMR-TMP). Moreover, from ssNMR emerged that the nature of the metal cation played a fundamental role influencing the strength of the Lewis acid sites with Hf presenting the strongest acidity.

FT-IR of adsorbed ammonia was employed as well to analyze the distribution of Brønsted and Lewis sites in the studied materials. Figure 5 presents the low-frequency region of the FT-IR difference (with the spectrum of the bare outgassed sample subtracted) normalized spectra of Ti—HNT-110, Zr—HNT-110, and Hf—NT-110 after exposure to ammonia and prolonged outgassing under dynamic vacuum ($P < 1.10^{-3}$ mbar, approximately 15 min). The remaining signals after outgassing were attributed to ammonia irreversibly adsorbed on the surfaces of the three samples. These signals indicated interactions of the probe molecules with Brønsted or Lewis sites, as well as ammonia chemisorbed on the silica surface. Notably, the broad band at 1460 cm^{-1} was associated with the bending mode of NH_4^+, resulting from ammonia protonation at Brønsted sites. The presence of this band was observed in all three samples, though with significant differences in intensity. Given that the spectra were normalized on silica overtone modes, these differences could be attributed to varying populations of Brønsted acidity. This acidity was most likely attributed to hydroxyl groups (Si—OH) coordinated to unsaturated M^{4+} cations on the surface of metal oxide clusters, which were acidic enough to protonate ammonia.

At higher wavenumbers, around 1550 cm^{-1}, a signal attributed to ammonia chemisorbed on siloxane groups was observed, indicating the formation of Si—NH_2 and Si—OH. This reactivity was more pronounced in Ti—HNT-110 compared to the other two samples. The contributions at 1608 cm^{-1} for Ti—HNT-110 and 1612 cm^{-1} for Zr—HNT-110 and Hf—NT-110 are due to ammonia adsorbed on unsaturated M^{4+} cations, which are sources of Lewis acidity.

Table 4. Catalytic activity of M(IV)-doped silica nanotubes in the conversion of ethyl levulinate to GVL.

Entry	Catalyst	Conversion (%)	Yield (%)	Sel. (%)	TON	$TON_{A.S.}$
1	Ti-NT-110	<2	<2	n.a.	n.a.	n.a.
2	Zr-NT-110	26	21	83	14	57
3	Hf-NT-110	50	38	77	26	80
4	Hf-NT-110	56	51	90	35	108
5	Hf-NT-110	79	61	77	42	128

Conditions of the catalytic tests (Entries 1 to 3): in Schlenk flask, 100 mg of catalyst, 150 °C, 3 h, 1 mmol of EL and 5 mL of ^{i}PrOH. Conditions of the catalytic test Entry 4: in pressurized reactor (Pi = 10 bar), 100 mg of catalyst, 150 °C, 3 h, 1 mmol of EL and 5 mL of iPrOH. Conditions of the catalytic test Entry 5: in Schlenk flask, 100 mg of catalyst, 150 °C, 3 h, 1 mmol of EL and 2.5 mL of iPrOH. The error on the yield is around 2% in absolute value. Sel. = Selectivity. TON = n_{GVL}/n_{M}; $TON_{A.S.}$ = $n_{GVL}/n_{acid\ sites}$; the amount of M (ICP-OES) within the M-doped samples was in the range 1.4–1.6 × 10^{-4} mol/g. n.a.: not applicable.

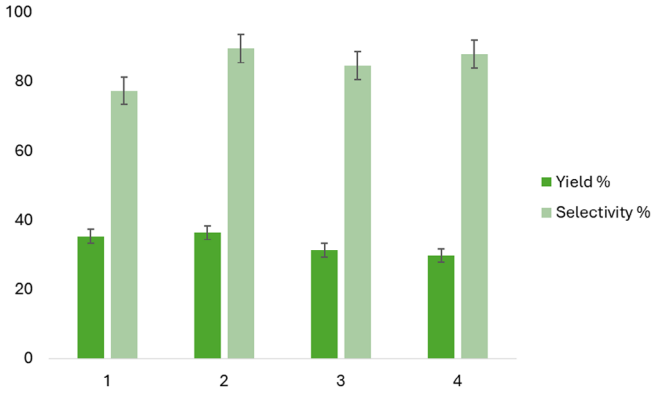

Figure 6. Recycling of Hf-NT-110 in Schlenk flask. Conditions of the catalytic tests: 100 mg of catalyst, 150 °C, 3 h, 1 mmol of EL and 5 mL of iPrOH. The catalyst was recovered with the minimum amount of isopropanol, filtered and calcined at 550 °C for 5 h. The amounts of reagents were adapted for every cycle on the basis of the quantity of catalyst recovered.

For Zr-HNT-110 and Hf-NT-110, a negative band (indicating species consumed by ammonia adsorption) was observed around 1580–1590 cm^{-1} (labelled with an * in Figure 5), complicating the evaluation of the intensity of bands attributed to ammonia on Lewis sites and the consequent quantification. To better understand the nature of these species perturbed by ammonia adsorption, the spectra of Ti—HNT-110, Zr—HNT-110, and Hf—NT-110 were compared after outgassing at 673 K (before ammonia dosage) to highlight potential differences in surface reactivity.

Figure S11 shows the low-frequency region spectra, where Zr—HNT-110 and Hf—NT-110, unlike Ti—HNT-110, had a shoulder at around 1590 cm^{-1}. This shoulder was assigned to the O—C—O stretching of chelating bidentate carbonate-like species, which formed on the surface of ZrO_2 when CO_2 reacts with adjacent Zr^{4+}-O^{2-} acid-base pairs (S10).[37] This reaction is expected on the surfaces of Zr—HNT-110 and Hf—NT-110, either from the thermal decomposition of precursors during calcination or from atmospheric CO_2 adsorption. The interaction of ammonia with Zr^{4+} (or Hf^{4+}) acid sites could perturb (or even displace) these bidentate carbonate species, producing the overlapped negative band and the broad band at higher wavenumbers. This observation provided additional evidence of the higher surface reactivity of Zr and Hf clusters compared to the Ti-containing sample in perfect agreement with the previous findings.

3.3. M(IV)-Doped Silica Nanotubes: Catalytic Results

The two newly obtained solids (Ti- and Hf-NT-110) were tested as catalysts for the conversion of EL to GVL and their performances were compared to the ones of Zr-NT-110 described above. Among the M—NT-110 series, it is immediately evident that Ti—NT-110 was not active for the target reaction (Entry 1, Table 4). This could be ascribed to the particularly weak acidity observed for this sample (see Section 3.2), although it was the one presenting the highest L/B ratio (last column of Table 3). Zr-NT-110 and HfNT-110 were both active with the latter catalyst displaying outstanding catalytic performance in terms of turnover number (compare Entries 2 and 3 on Table 4). The enhanced catalytic activity of Hf-NT-110 could be ascribed to a combination of favorable features such as the overall quantity of acid sites, a high L/B ratio together with the presence of strong Lewis sites at the surface. It was previously shown that the higher the L/B ratio, the better the performances of the catalyst.[38] Herein, another important piece was added to improve the overall understanding: the strength of the acid sites plays a key role in the catalytic activity of the solids. The excellent catalytic performance of Hf-NT-110 is even more evident if the TON is calculated taking into account the overall acidity (TON acid sites: $TON_{A.S.}$). The catalytic data of the different M—NT-110 catalysts after 3, 6, and 24 h reaction are available in supporting information (Table S1).

To assess the stability of the best catalyst of the series, namely Hf—NT-110, under the selected reaction conditions, a hot filtration was carried out. The catalyst was separated from the reaction mixture via filtration after 3 h and the supernatant was stirred for an additional 3 h under the same reaction conditions. By analyzing the supernatant right after the filtration and after 6 h, it was possible to conclude that the yield of the reaction remained constant after the catalyst removal (see Figure S12). This proved that the solid was not leaching active sites and that it was stable under the selected reaction conditions.

Recyclability is one of the key features that a heterogeneous catalyst should possess. Hf—NT-110 was successfully reused for four consecutive cycles (see Figure 6). After each cycle the catalyst was recovered from the flask with the minimum amount of solvent (isopropanol) and it was calcined at 550 °C for 5 h. A slight decrease in yield was observed between the second and the third cycle and was followed by a stabilization of the catalytic performances thus confirming the robustness of the catalyst under the selected conditions. TEM analysis of the solid after the last cycle was carried out to prove that the tubular

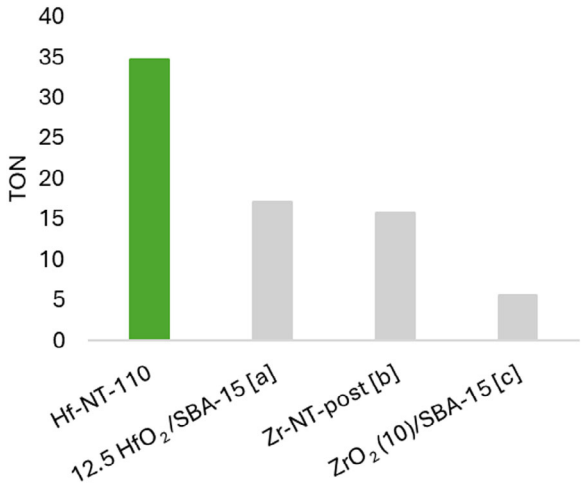

Figure 7. Comparison of TON obtained with the best catalyst in this work with other mesoporous silica-based materials reported in literature. [a][41] [b][18] [c].[40]

morphology of the catalyst was preserved (see Figure S13). N_2 physisorption measurements and ICP-OES analysis of the reused catalyst evidenced no modification of textural properties and of metal content during catalysis (Figure S13).

The E-factor of the reaction employing Hf—NT-110 as catalyst was calculated as the ratio between the mass of waste produced and the mass of product obtained. The conditions in which the catalytic test was carried out for this estimation were: 70 mg of catalyst, 150 °C, 24 h, 0.7 mmol of EL and 3.5 mL of iPrOH. The excess of solvent was recovered at the end of the reaction via a microdistillation apparatus. The formula applied for the calculation of the E-factor was: [(0.10 g EL + 2.75 g iPrOH − 2.39 g recovered iPrOH − 0.06 g GVL)/0.06 g GVL] = 6.7. Note that the catalyst is not included in the formula because it is reusable. The value obtained is very close to the limit of the range for the production of bulk chemicals, indicating that this catalyst is promising also from a sustainability viewpoint.[39]

The catalytic tests reported above were carried out in a 10 mL Schlenk flask, where the reaction proceeded under autogenous pressure. To evaluate the impact of the pressure, additional catalytic tests within a sealed reactor were performed as well. Hf—NT-110, was selected to perform a test in a pressurized reactor, setting 10 bar as initial pressure (P_i). This resulted in the improvement of the yield and, more importantly, of the selectivity towards the formation of GVL, as emerged from the comparison between Entry 3 and Entry 4 in Table 4. The catalytic performances of the solid employing the pressurized reactor allowed us to compare its activity with some materials previously reported in literature (see Figure 7) and tested under the same conditions (except for "12.5HfO_2/SBA-15" that was tested at P_i = 8 bar and T = 120 °C). As shown in Figure 7, Hf—NT-110 outperformed other catalysts already reported in the literature. A more direct comparison can be done with hollow silica nanotubes reported by Soumoy et al.[18] (namely "Zr-NT-post"). From this comparison clearly emerged that the presence of Hf combined with a tuned Si/M ratio plays a key role in enhancing the performance of the catalyst. Moreover, considering another kind of mesoporous silica material, namely SBA-15, impregnated with ZrO_2[40] or HfO_2,[41] it is evident that hollow silica nanotubes are more active towards the conversion of ethyl levulinate to γ-valerolactone, in terms of TON.

Moreover, it was possible to further improve the performance of the catalyst by performing a test with half of the amount of solvent (namely 2.5 mL instead of 5 mL), as shown in Entry 5 of Table 4. In this way the TON of the catalyst increased to 42 and the $TON_{A.S.}$ reached the value of 128, revealing once again the excellent activity obtainable using Hf-NT-110 as catalyst for the target reaction.

4. Conclusion

A post-synthesis procedure was successfully employed to obtain metal(IV)-doped hollow silica nanotubes (M—NT) acting as efficient catalysts for the conversion of ethyl levulinate into GVL. All the solids presented a well-defined tubular morphology, high specific surface areas (from 450 to 570 m^2/g) and both micro- and meso-porosity. Two series of materials were synthesized, namely Zr-NT-*x* (where x is the theoretical Si/M ratio) and M-NT-110 (M = Ti, Zr, Hf). In the first case, different Si/Zr were targeted, i.e., 37, 74, and 110. The excellent correspondence between the experimental and the theoretical Si/Zr values was assessed via ICP-OES measurements, while the interaction between the metal centers and the silica structure was confirmed by XPS analyses. A first screening of the catalytic activities of these solids led to conclude that Zr-NT-110 was the best catalyst of the series, most probably because it constitutes the best compromise between a fine dispersion of the metal oxides and a sufficient amount of active sites within the material. Then, two other materials were synthesized: Ti-NT-110 and Hf-NT-110. Their textural and chemical properties, assessed via TEM, N_2 physisorption, ICP-OES and XPS measurements, did not reveal relevant differences among the samples, while from acidity measurements, namely TPD of ammonia, FT-IR of adsorbed ammonia and ^{31}P ss-NMR of adsorbed TMP, some key differences emerged. On the one hand, ammonia TPD showed that Ti-NT-110 displayed the weakest acidic sites of the series, while Zr-NT-110 and Hf—NT-110 possessed similar total acid strength. On the other hand, ^{31}P ss-NMR of adsorbed TMP was the key technique to gain more insights on the nature of the acid sites. These results allowed explaining the catalytic activity of the solids. Indeed, Ti-NT-110 active sites are not strong enough to convert EL to GVL, leading to very poor yields of GVL. By contrast, Hf-NT-110, which displayed stronger Lewis acid sites than Zr-NT-110, as emerged from ss-NMR analysis of adsorbed TMP, was the best one of the series in terms of TON. FT-IR of adsorbed ammonia confirmed the results obtained via NMR. The best solid was proven to be stable under the reaction conditions, recyclable for four consecutive cycles and very promising for the conversion of ethyl levulinate to γ-valerolactone if compared to other similar catalysts reported in literature. This demonstrates that a combination of strong Lewis acid sites, high L/B ratio and finely dispersed oxide clusters on high surface area nanostructured silica, is essential to obtain very promising active catalysts for this reaction.

Acknowledgements

Authors acknowledge the FNRS for the financial support in the context of the FRIA PhD grants of A. Maertens and L. Soumoy and the EOS funding scheme for the PhD grant of M. Saitta. This project received funding from the FWO and F.R.S.-FNRS (Belgium) under the Excellence of Science (EOS) program ("PHOSPORE" – EOS reference number: 40,007,504) as well as from the FNRS via a PdR project (ref: T.0004.21). This research used resources of PC^2 (Physico-Chemical Characterization), MORPH-IM (Morphology & Imaging), and SIAM (Synthesis, Irradiation & Analysis of Materials) technology platforms located at the University of Namur. This research also used resources of the Institute of Condensed Matter and Nanosciences (IMCN) at Université catholique de Louvain (UCLouvain) to conduct the ammonia temperature-programmed desorption coupled with mass spectrometry analysis. The IR measurements were performed at the Polytechnic of Turin.

Conflict of Interests

The authors declare no conflict of interest.

Data Availability Statement

The data that support the findings of this study are available from the corresponding author upon reasonable request.

Keywords: Biomass conversion · Heterogeneous catalysis · Hollow silica nanotubes · Lewis/Brønsted acid balance · Mesoporous materials

[1] a) A. Corma, S. Iborra, A. Velty, *Chem. Rev.* **2007**, *107*, 2411–2502; b) N. Romano, in *Enzymes in Human and Animal Nutrition* (Eds: V. Kumar, C. S. Nunes), Academic Press, Amsterdam **2018**, pp. 381–396.
[2] A. Yousuf, D. Pirozzi, F. Sannino, in *Lignocellulosic Biomass to Liquid Biofuels* (Eds: A. Yousuf, D. Pirozzi, F. Sannino), Academic Press, Amsterdam **2020**, pp. 1–15.
[3] L. Ye, Y. Han, J. Feng, X. Lu, *Ind. Crops Prod.* **2020**, *144*, 112031.
[4] I. T. Horváth, H. Mehdi, V. Fábos, L. Boda, L. T. Mika, *Green Chem.* **2008**, *10*, 238–242.
[5] a) C. E. Chan-Thaw, M. Marelli, R. Psaro, N. Ravasio, F. Zaccheria, *RSC Adv.* **2013**, *3*, 1302–1306; b) Z. Vobecka, C. Wei, K. Tauer, D. Esposito, *Polymer* **2015**, *74*, 262–271.
[6] T. Raj, K. Chandrasekhar, R. Banu, J.-J. Yoon, G. Kumar, S.-H. Kim, *Fuel* **2021**, *303*, 121333.
[7] W. R. H. Wright, R. Palkovits, *ChemSusChem* **2012**, *5*, 1657–1667.
[8] B. Banerjee, R. Singuru, S. K. Kundu, K. Dhanalaxmi, L. Bai, Y. Zhao, B. M. Reddy, A. Bhaumik, J. Mondal, *Catal. Sci. Technol.* **2016**, *6*, 5102–5115.
[9] K. Dhanalaxmi, R. Singuru, S. Mondal, L. Bai, B. M. Reddy, A. Bhaumik, J. Mondal, *ACS Sustainable Chem. Eng.* **2017**, *5*, 1033–1045.
[10] A. Osatiashtiani, A. F. Lee, K. Wilson, *J. Chem. Technol. Biotechnol.* **2017**, *92*, 1125–1135.
[11] H. Y. Luo, J. D. Lewis, Y. Román-Leshkov, *Annu. Rev. Chem. Biomol. Eng.* **2016**, *7*, 663–692.
[12] a) M. Chia, J. A. Dumesic, *Chem. Commun.* **2011**, *47*, 12233–12235; b) P. B. Vásquez, T. Tabanelli, E. Monti, S. Albonetti, D. Bonincontro, N. Dimitratos, F. Cavani, *ACS Sustainable Chem. Eng.* **2019**, *7*, 8317–8330; c) T. Tabanelli, E. Paone, P. Blair Vásquez, R. Pietropaolo, F. Cavani, F. Mauriello, *ACS Sustainable Chem. Eng.* **2019**, *7*, 9937–9947.
[13] M. Cabanillas, A. Franco, N. Lázaro, A. M. Balu, R. Luque, A. Pineda, *Molecular Catal.* **2019**, *477*, 110522.
[14] S. S. Enumula, V. R. B. Gurram, M. Kondeboina, D. R. Burri, S. R. R. Kamaraju, *RSC Adv.* **2016**, *6*, 20230–20239.
[15] J. Lai, S. Zhou, X. Liu, Y. Yang, J. Lei, Q. Xu, D. Yin, *Catal. Lett.* **2019**, 149.
[16] A. H. Valekar, K.-H. Cho, S. K. Chitale, D.-Y. Hong, G.-Y. Cha, U. H. Lee, D. W. Hwang, C. Serre, J.-S. Chang, Y. K. Hwang, *Green Chem.* **2016**, *18*, 4542–4552.
[17] a) B. Tang, S. Li, W.-C. Song, E.-C. Yang, X.-J. Zhao, N. Guan, L. Li, *ACS Sustainable Chem. Eng.* **2019**, *7*, 16329–16343; b) H. Y. Luo, D. F. Consoli, W. R. Gunther, Y. Román-Leshkov, *J. Catal.* **2014**, *320*, 198–207.
[18] L. Soumoy, A. Maertens, A. Morena, L. Fusaro, M. Armandi, S. Fiorilli, D. P. Debecker, C. Aprile, *Mater. Tod. Chem.* **2024**, *40*, 102189.
[19] M. Shamzhy, M. Opanasenko, P. Concepción, A. Martínez, *Chem. Soc. Rev.* **2019**, *48*, 1095–1149.
[20] W. Wu, Y. Li, H. Li, W. Zhao, S. Yang, *Catalysts* **2018**, *8*, 264.
[21] J. K. F. Buijink, J. J. M. van Vlaanderen, M. Crocker, F. G. M. Niele, *Catal. Tod.* **2004**, *93*, 199–204.
[22] V. Smeets, E. M. Gaigneaux, D. P. Debecker, *ChemCatChem* **2022**, *14*, e202101132.
[23] T. Yang, H. Li, J. He, Y. Liu, W. Zhao, Z. Wang, X. Ji, S. Yang, *ACS Omega* **2017**, *2*, 1047–1054.
[24] D. Zhao, T. Su, D. Rodríguez-Padrón, H. Lü, C. Len, R. Luque, Z. Yang, *Mater. Tod. Chem.* **2022**, *24*, 100745–100757.
[25] Y. Zhou, J. He, R. Chen, X. Li, *Mater. Tod. Sustain.* **2022**, *18*, 100138.
[26] C. Zhou, W. Deng, X. Wan, Q. Zhang, Y. Yang, Y. Wang, *ChemCatChem* **2015**, *7*, 2853–2863.
[27] L. Lisuzzo, W. F. Stickle, P. E. Sobol, K. D. Bomben, G. Cavallaro, D. Duca, F. Ferrante, *ACS Catal.* **2024**, *14*, 18167–18203.
[28] R. M. Bullock, J. G. Chen, L. Gagliardi, P. J. Chirik, O. K. Farha, C. H. Hendon, C. W. Jones, J. A. Keith, J. Klosin, S. D. Minteer, R. H. Morris, A. T. Radosevich, T. B. Rauchfuss, N. A. Strotman, A. Vojvodic, T. R. Ward, J. Y. Yang, Y. Surendranath, *Science* **2020**, *369*, eabc3183.
[29] L. Soumoy, L. Fusaro, D. P. Debecker, C. Aprile, *Chem. Mater.* **2023**, *35*, 1877–1890.
[30] L. Huang, M. Kruk, *Chem. Mater.* **2015**, *27*, 679–689.
[31] L. Soumoy, C. Célis, D. P. Debecker, M. Armandi, S. Fiorilli, C. Aprile, *J. Catal.* **2022**, *411*, 41–53.
[32] J. F. Moulder, W. F. Stickle, P. E. Sobol, K. D. Bomben, in *Handbook of X-ray Photoelectron Spectroscopy* (Ed: J. Chastain), Perkin-Elmer Corporation, Eden Prairie, MN **1992**.
[33] A. Zheng, S.-B. Liu, F. Deng, *Chem. Rev.* **2017**, *117*, 12475–12531.
[34] X. Yi, Y.-K. Peng, W. Chen, Z. Liu, A. Zheng, *Acc. Chem. Res.* **2021**, *54*, 2421–2433.
[35] S. Song, L. Di, G. Wu, W. Dai, N. Guan, L. Li, *Appl. Catal. B: Environ.* **2017**, *205*, 393–403.
[36] X. Yi, H.-H. Ko, F. Deng, S.-B. Liu, A. Zheng, *Nat. Protoc.* **2020**, *15*, 3527–3555.
[37] J. C. Lavalley, *Catal. Tod.* **1996**, *27*, 377–401.
[38] J. M. Guarinos, F. G. Cirujano, A. Rapeyko, F. X. Llabrés i Xamena, *Molecular Catal.* **2021**, *515*, 111925.
[39] R. A. Sheldon, M. L. Bode, S. G. Akakios, *Curr. Opin. Green Sustainable Chem.* **2022**, *33*, 100569.
[40] Y. Kuwahara, W. Kaburagi, Y. Osada, T. Fujitani, H. Yamashita, *Catal. Tod.* **2017**, *281*, 418–428.
[41] C. Cai, Z. Liu, X. Wang, Z. Wen, B. Yan, B. Xue, *Catal. Tod.* **2024**, *441*, 114902.

Manuscript received: December 22, 2024
Revised manuscript received: February 13, 2025
Accepted manuscript online: February 27, 2025
Version of record online: ■■, ■■